Deep-Sea Research Part II xxx (xxxx) xxx–xxx

Contents lists available at ScienceDirect

Deep-Sea Research Part II

journal homepage: www.elsevier.com/locate/dsr2

Nontronite-bearing tubular hydrothermal deposits from a Galapagos seamount

Megan Lubetkin[a,b,*], Steven Carey[b], Katherine A. Kelley[b], Geneviève Robert[a], Winton Cornell[c], Nicole Raineault[d], Jacob Balcanoff[b], Robert D. Ballard[b,d], Pelayo Salinas-de-León[e,f]

[a] Department of Geology, Bates College, Lewiston, ME, United States
[b] Graduate School of Oceanography, University of Rhode Island, Narragansett, RI, United States
[c] Department of Geosciences, University of Tulsa, Tulsa, OK, United States
[d] Ocean Exploration Trust, Narragansett, RI, United States
[e] Department of Marine Sciences, Charles Darwin Research Station, Puerto Ayora, Galápagos Islands, Ecuador
[f] Pristine Seas, National Geographic Society, Washington, D.C., United States

ARTICLE INFO

Keywords:
Galapagos
E/V Nautilus
Seamount
Nontronite
Hydrothermal vent
Biomineralization
Remotely operated vehicle
Telepresence

ABSTRACT

A telepresence-enabled cruise using remotely operated vehicle (ROV) exploration discovered an unusual tubular deposit of Fe-rich hydrothermal nontronite on a young seamount, Mashi, of the Wolf-Darwin lineament in the Galápagos Islands. X-ray diffraction, ICP-MS, ICP-AES, and SEM-EDS analyses show that this deposit is chemically and mineralogically similar to other deep-sea hydrothermal nontronites, indicating a likely formation temperature of about 30° to 50 °C by diffuse hydrothermal activity. These deposits contain mixtures of Fe-rich, Al-poor nontronite and poorly crystalline Fe-Si-oxyhydroxides with bulk compositions of 38–51 wt% SiO_2 and 40–50 wt% Fe_2O_3*. The presence of filamentous and spherical structures in the samples suggests that mineral deposition was in part facilitated by chemosynthetic microbes. Although hydrothermal nontronite has been sampled at a number of seafloor sites by coring and dredging, this is the first in situ documentation of its unusual sinuous, tubular structure, on the seafloor. Quantitative image-analysis of ROV imagery indicates that hydrothermal fluid pathways, developed through an underlying pillow lava sequence, likely control the distinctive sinuous morphology.

1. Introduction

1.1. Background

Nontronite, an Fe-rich smectite, is the most common clay mineral found at seafloor hydrothermal systems, yet it is typically not present in ancient volcanic sequences, suggesting that it undergoes transformation to other phases over long periods of time (Dekov et al., 2007). It most likely forms by precipitation from hydrothermal fluids at generally low temperatures (20–80 °C) in areas of diffuse flow (DeCarlo et al., 1983; Alt, 1988; Murname and Clague, 1983; Dekov et al., 2007). Low-temperature venting with nontronite and Fe-Si-oxyhydroxide (Fe-Si-oxide) formation has been documented at several seamounts throughout the world, notably Seamount 5 and the Red Seamount near the East Pacific Rise (EPR; Alt, 1988); Eolo Seamount in the Aeolian volcanic arc, Tyrrhenian Sea (Dekov et al., 2007); Loihi Seamount, Hawaiian archipelago (De Carlo et al., 1983; Emerson and Moyer, 2002); and the Kasuga 3 Seamount in the Northern Marianas (McMurtry et al., 1993). Most studies have recovered samples by dredging or coring and consequently there have been relatively few in situ observations of hydrothermal nontronite structure and morphology on the seafloor (De Carlo et al., 1983; Murnane and Clague, 1983; Alt, 1988; McMurtry et al., 1993; Dekov et al., 2007).

Understanding diffuse, low-temperature hydrothermal systems is important for evaluating geochemical exchanges between the seawater and the oceanic crust (Tivey, 2007). Focused high-temperature venting significantly contributes to the overall hydrothermal flux in the oceans, but diffuse flow has also been identified as a major process in marine geochemical cycling (Bemis et al., 2012). In addition, the presence of such systems may provide clues to the location of subsurface massive sulfide deposits, which are of economic significance (e.g. Murnane and Clague, 1983, Petersen et al., 2008).

* Corresponding author at: Graduate School of Oceanography, University of Rhode Island, Narragansett, RI, United States.
E-mail addresses: mjlubetkin@gmail.com (M. Lubetkin), scarey@uri.edu (S. Carey), kelley@uri.edu (K.A. Kelley), grobert@bates.edu (G. Robert), winton-cornell@utulsa.edu (W. Cornell), nicole@oceanexplorationtrust.org (N. Raineault), jbalcano117@gmail.com (J. Balcanoff), captainemo@comcast.net (R.D. Ballard), pelayo.salinas@fcdarwin.org.ec (P. Salinas-de-León).

http://dx.doi.org/10.1016/j.dsr2.2017.09.017

A telepresence-enabled expedition of the E/V *Nautilus* to the Galapagos Islands (NA064) in 2015 conducted remotely operated vehicle (ROV) explorations of seamounts to the north of the main Galapagos platform. With the Nautilus Live telepresence capabilities, researchers from the Galapagos and around the world were involved remotely in the shipboard science operations and dive planning.

Here, we report the discovery of an unusual low-temperature diffuse hydrothermal system that we explored and sampled near the summit of a seamount along the Wolf-Darwin lineament. The nontronite-bearing hydrothermal deposits consist of an extensive area of porous tubes developed in a sinuous pattern on the seafloor. In this paper, we report the major and trace element compositions of the deposits as determined by ICP-MS/ICP-AES and mineralogy inferred from X-ray diffraction. ROV imagery of the deposit and adjacent seafloor is used to develop an evolutionary model for the formation of the unusual sinuous depositional pattern. Evidence from scanning electron microscopy (SEM) also provides support for the important role of chemosynthetic microbes in facilitating mineral precipitation.

1.2. Geologic setting of the hydrothermal deposits

1.2.1. Galapagos islands and seamounts

The Galapagos Platform in the eastern Pacific consists of 20 volcanic islands and numerous seamounts (Geist et al., 2006). Its origin is tied to excess volcanism associated with a deep-seated mantle plume in close proximity to the Galapagos spreading center (GSC; Behn et al., 2004). Volcanic production of the hotspot over time has led to the creation of the paired Cocos and Carnegie Ridges on the Cocos and Nazca plates, respectively (O'Connor et al., 2007). The northern part of the Galapagos Platform includes several linear chains of seamounts that extend northwards towards the GSC and lie generally subparallel to the NW-SE trending Galapagos fracture zone (Fig. 1). The Wolf-Darwin lineament, consisting of two islands and three seamounts, lies furthest to the west and is the site of the youngest recorded seamounts of the region (≤1 Ma; Sinton et al., 1996). No well-defined age progression occurs along the lineament and the volcanism may be controlled by deep-seated lithospheric weaknesses that are exploited by faulting and stress from the nearby transform boundary and ridge interaction (Sinton et al., 1996).

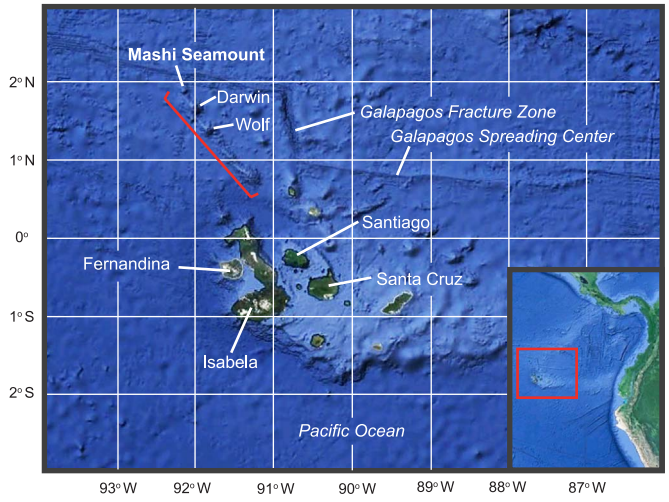

Fig. 1. The Galapagos Island platform and adjacent Galapagos Spreading Center to the north. Location of Mashi Seamount is shown in the northwest part of the Wolf-Darwin lineament (highlighted by the red bracket). Inset map on the lower right shows position of the Galapagos Islands relative to South America. (Basemap created from Google Earth). (For interpretation of the references to color in this figure legend, the reader is referred to the web version of this article).

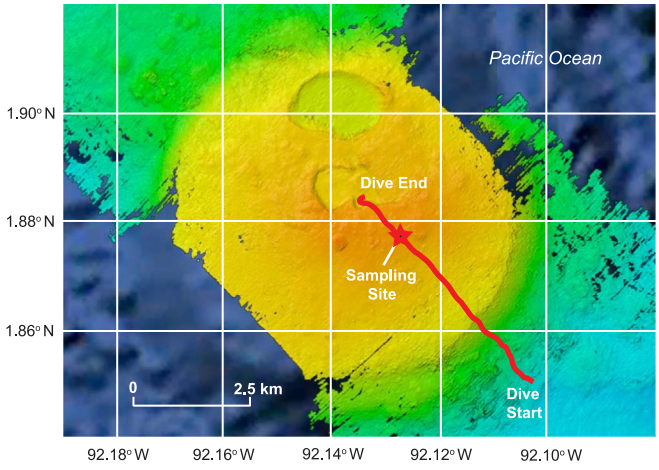

Fig. 2. Multibeam map of Mashi Seamount showing ROV *Hercules* dive track (red) during dive H1440. Location of site where samples for this study were collected is indicated by the star. Water depth at start of dive was 1960 m and end of dive was 1324 m. (Multibeam data acquired onboard E/V *Nautilus* using the hull-mounted EM302 echosounder; data courtesy of the Ocean Exploration Trust). (For interpretation of the references to color in this figure legend, the reader is referred to the web version of this article).

1.2.2. Mashi Seamount

Mashi Seamount is a prominent and relatively young (~0.8–0.9 Ma; Sinton et al., 1996) flat-topped seamount to the northwest of Darwin Island (Fig. 2). Mashi is about 735 m high with its summit at a depth of about 1225 m and its base at about 1960 m. It was explored by ROVs during dive H1440 of cruise NA064 (E/V *Nautilus*) in 2015 (see Fig. 2 for vehicle dive track). The base of Mashi is generally covered by fine-grained sediment with isolated pillow lava outcrops that gradually transition going upslope to patches of talus blocks. Along its southeastern slope there are extensive areas of steep lava talus that grade into alternating outcrops of pillow lava and areas of pelagic sediment cover towards the summit. A series of at least four nested craters with diameters up to 2 km occur in the central and northern part of Mashi's relatively flat-topped summit (Fig. 2).

1.2.3. Hydrothermal deposit structure and morphology

Sinuous, tubular hydrothermal deposits occur near the summit of Mashi at a depth of 1227 m (star in Fig. 2). This tubular network is partially covered by sediment and is colonized by sparse sponges and deep-sea corals. The patterned network of deposits becomes gradually denser as the sediment cover diminishes toward the summit. Typically the hydrothermal deposits consist of approximately 20 cm diameter overlapping tubes that are porous and friable with yellowish microbial mat growing along fractures and crevices. Use of the two-vehicle ROV system (*Hercules* and *Argus*) enabled simultaneous imagery both from above (about 10–15 m over the seafloor) and close-up to the deposits (1–2 m from seafloor; Fig. 3). Attempted sampling using the ROV manipulator arm resulted in breakage of the tubes, revealing the fragile interiors. The tubes are strongly zoned with a bright green interior grading outwards to an orange-red crust with a darker black outer crustal layer (Fig. 4). Two samples were collected using the ROV (Table 1): sample NA064-064 was of the yellow microbial mat covered deposits, which included some of the green interior, orange-red exterior, and dark crust. However, these layers were not nearly as distinct as they were in sample NA064-065 which was another grab sample of the deposits in the same general area. NA064-065 recovered all three of these major layers quite distinctly (Fig. 4).

2. Material and methods

Samples were air-dried, photographed and described in the E/V *Nautilus* wet lab. Each sample was further divided based on visual

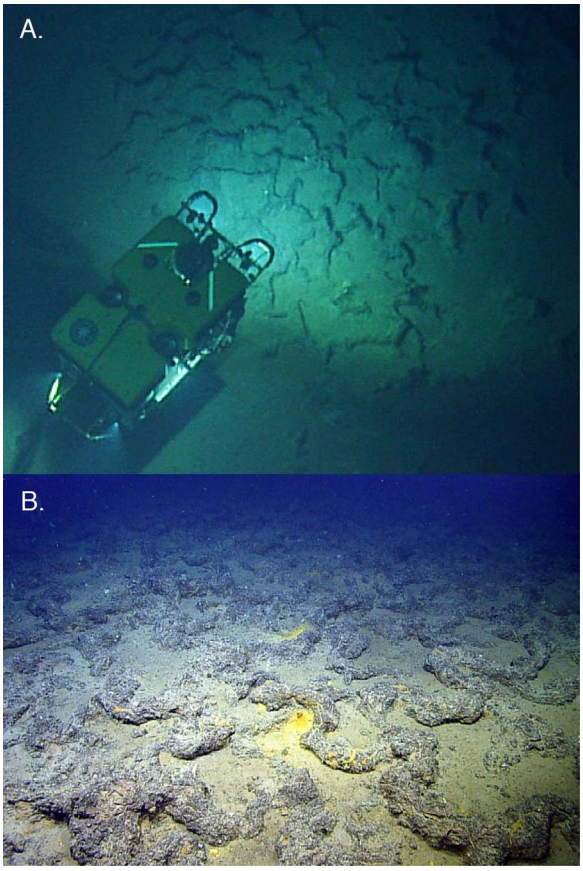

Fig. 3. A. Downward looking view from ROV *Argus* above ROV *Hercules* (lower left in image) showing the pattern of the tubular hydrothermal deposits. Distance to the seafloor from *Argus* is about 15 m. For scale, *Hercules* is 1.73 m wide and 3.86 m long. B. Tube-like hydrothermal deposits near the summit of Mashi Seamount. Tube diameter in the center of the image is about 20 cm. Yellow microbial mat is present in center of the image. Images from dive H1440 of cruise NA064. (For interpretation of the references to color in this figure legend, the reader is referred to the web version of this article).

examination and color into four sub-samples: green indurated clay (NA064-064A; NA064-065A), bright orange rusty fine silt/clay (NA064-064B; NA064-065B), poorly indurated dark banded clay from the crust of the deposits (NA064-064C; NA064-065C), and remaining bulk sample (NA064-064D; NA064-065D). Each sub-sample was further split into a whole aliquot for SEM-EDS analysis. A second split for X-ray diffraction (XRD) analysis was powdered in a Spex Mixer Mill, then ground wet in a mortar and pestle with ethanol, air-dried and placed in a desiccator for one week. XRD sub-samples were ground in a mortar and pestle a second time (dry) to a fine powder.

The mineralogy of the powdered samples was characterized by XRD, energy-dispersive X-ray spectroscopy (EDS), and scanning electron microscopy (SEM). Powder mounts were scanned with a Rigaku MiniFlex II Desktop X-ray Diffractometer using Cu K_α radiation, 30 kV, 15 mA from 2 to 80° 2θ, 0.8°/min (0.04°/step and 3 s/step). Carbon-coated specimens were analyzed by EDS analysis and gold-palladium-coated specimens were imaged by SEM on a JEOL JSM-7100FLV with a Noran System 7 EDS System. Details of the sample preparation techniques for XRD and geochemical analyses are provided in the Appendix A.

Major element compositions of the powders were determined by inductively coupled plasma atomic emission spectroscopy (ICP-AES) using a Perkin Elmer Optima 3100 XL spectrometer. Trace elements and selected major elements (K, P) of the powders were determined by inductively coupled plasma mass spectrometry (ICP-MS) using a Thermo X-Series II quadrupole ICP-MS. Standards and run conditions for both ICP methods were adopted from Kelley et al. (2003).

Image analysis was performed using nine screen-captures from the HD video feed captured by ROV *Hercules* during dive H1440 on Mashi for the purpose of comparing spatial dimensions of hydrothermal deposits to associated pillow lava. Six images of the overlapping tubular pattern of the deposits were selected from both close-up *Hercules* views and more distal *Argus* views. Three images from nearby pillow lava formations were selected at similar scales. Adjustments for image parallax were not taken into account because the vehicle was relatively close to the bottom during imaging. The boundaries of the hydrothermal tubes and individual pillow lobes were outlined and then the major and minor axis of the features were measured in Adobe Illustrator and scaled to the dimensions of the ROV in the images.

3. Results

3.1. Mineralogy (X-ray diffraction)

Analysis of X-ray diffractograms of sub-samples NA064-64A, NA064-64B, NA064-64C, NA064-65A, NA064-65B, and NA064-65C reveals an overall diffraction pattern similar to that of many hydrothermal nontronites (Fig. 5) (DeCarlo et al., 1983; Murnane and Clague, 1983). All six subsamples (A-B-C) show patterns with little variability between diffractograms. The sub-samples of green clay, NA064-64A and NA064-65A, display nearly identical patterns with prominent smectite peaks at 6.7, 19.4, 27.3, 34.8, 53.7, and 61.7 (2θ values, Fig. 5). The diffractograms for NA064-64C and NA064-65C follow the same pattern as those of NA064-64A and NA064-65A but with lower intensity peaks. The diffractogram of NA064-65B is considerably different than that of the other five sub-samples. It lacks many of the distinctive smectite peaks and resembles the overall trend for poorly crystalline Fe-oxyhydroxides (e.g. DeCarlo et al., 1983). In the sub-samples of the dark crustal material (NA064-64C and NA064-65C), there is a small but noticeable peak around 12° 2θ (Fig. 5) that is attributed to a 7-Å Mn-oxide mineral (Murnane and Clague, 1983).

A simulated (Rietveld refinement) comparison of true nontronite with the diffractograms of each sub-sample indicate a clear dominance of smectite peaks (nontronite) in the crystalline assemblage (Fig. 5) but trace and major element data presented later in the paper strongly suggest the presence of other amorphous phases that could not be detected by XRD.

3.2. SEM-EDS imaging

A general sponge-like structure of the green clay is displayed in SEM images of sub-sample NA064-64A (Fig. 6A). This spongy basic structure (Fig. 6A) appears to be porous while consisting of many micro-tube aggregates that are visible at higher magnifications (Fig. 6B-C) and are similar to those shown by Köhler et al. (1994). Sub-sample NA064-65A exhibits hollow branching filamentous micro-tubes that zigzag, stack, and overlap (Fig. 6B-C). These tubular filaments of about 2–5 μm in diameter consist of flat overlapping sheets and were most notably observed in specimens from NA064-65A and NA064-65B. Similar overlapping fine folded clay-sheets were observed in nontronite samples from Köhler et al. (1994). EDS analysis of these structures shows that they consist of more than 40 wt% SiO_2, nearly 50 wt% Fe_2O_3*, and contain lesser amounts of Na_2O, MgO, and K_2O (about 2–7 wt% for each).

Fig. 6D shows a close up of the web-like spongy structure of the orange sub-sample NA064-64B. Spherical bulbs with diameters at about 2–10 μm exhibit central hollow features (Fig. 6E). These microspheres with central indents are extremely rich in Fe_2O_3* (about 85 wt%) and poor in SiO_2 (about 0.5 wt%) (Fig. 6E). The microspheres also contain almost 3 wt% MnO, and trace amounts of Al_2O_3, CaO, and C. NA064-64B has a high Fe_2O_3* content with relatively high MnO fitting the possibility of a Mn-oxide crust interlayered with Fe-oxide nodules. Other images from NA064-64B show broken hollow filaments about

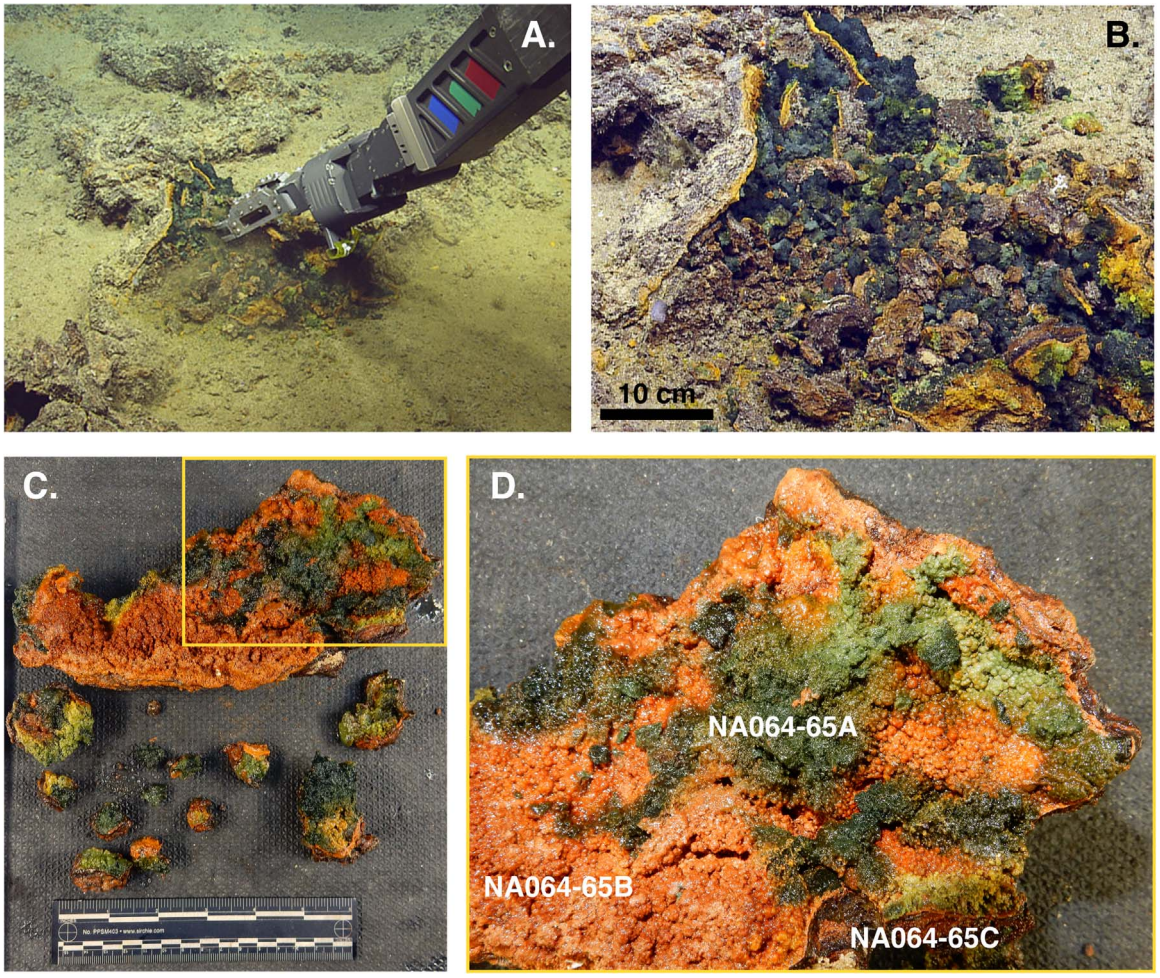

Fig. 4. A. Sampling of hydrothermal deposits by ROV *Hercules* during dive H1440 in the Galapagos Islands. B. Close up of the broken interior of a hydrothermal tube showing a strong gradation in color from deep green in the interior to yellow-orange on the exterior crust. Scale bar derived from the two red laser dots in the upper central part of the image that are 10 cm apart. C. Sample NA064-065 interlayered and very friable. Bright green interior, yellow-orange material moving outward with a dark thin outer crust. D. Magnified view of the left yellow box in C with labeled sub-sample regions. Similar sub-sample divisions were made for sample NA064-64 (A, B, C, and D). (For interpretation of the references to color in this figure legend, the reader is referred to the web version of this article).

Table 1
Sample identification with corresponding location coordinates, water depths, and general description of appearance.

Sample ID	Latitude (°N)	Longitude (°W)	Depth (m)	Description
NA064-064 NA064-065	1.876603 1.876802	92.1271104 92.1270681	1227.26 1226.31	Tubular pattern of friable Fe-rich low-temperature hydrothermal crust; bright orange and green interior color with a darker outer layer

1 μm in diameter (Fig. 6F).

Sample NA064-65A also exhibits oblate microspheres that are coated in finely layered sheets (Fig. 6G). These structures do not have central indents and contain over 24 wt% SiO_2, nearly 70 wt% Fe_2O_3*, and trace amounts of Na_2O, MgO, K_2O, and C (> 0.5 wt% for each).

Several other SEM images from sub-sample NA064-64B show structures that resemble morphologies of Fe-oxides, nontronite, and possible associated microbial remnants (Fig. 6H and I). One area of the sample includes several regions of stacked Fe-oxide encrusted filaments (Fig. 6I) that are similar to filaments produced by Fe-oxidizing bacteria (Dekov et al., 2010, 2007). Among these stacks are oblate microspheres that propagate off of the filaments (Fig. 6H and I). EDS analysis indicates that the filaments, such as those shown in Fig. 6I, have about 10 wt% SiO_2, nearly 74 wt% Fe_2O_3*, almost 8 wt% P_2O_5, and trace amounts of Na_2O, MgO, CaO, Cl, and C. More oblate spheres were observed in other areas of NA064-64B.

3.3. Major element composition

Compared with deposits from other vent sites (Hekinian et al., 1978; Dymond and Eklund, 1978; Corliss et al., 1978; Grill et al., 1981; Murnane and Clague, 1983; De Carlo et al., 1983; Alt et al., 1987; Cole, 1988; Stoffers et al., 1990; McMurtry et al., 1993; Severmann et al., 2004; Dekov et al., 2007), the Mashi Seamount samples exhibit enrichment in Fe_2O_3* relative to SiO_2 (Fig. 7; Table 2). We attribute this enrichment to the samples representing mixtures of both nontronite and Fe-oxides, as suggested by the XRD analysis. Overall, the deposits contain 38–51 wt% SiO_2 and 40–50 wt% Fe_2O_3*. Sub-samples NA064-64A and NA064-65A are the most SiO_2-rich and lowest in Fe_2O_3 while NA064-65B is the least SiO_2-rich and the highest in Fe_2O_3. MnO is most abundant in the exterior crust sub-samples (NA064-64C and NA064-65C) and the bulk samples (NA064-64D and NA064-65D), consistent with the presence of a Mn-oxide phase as observed in the XRD data (Fig. 5). MgO and Na_2O are present at low abundance in all sub-samples (1.5–2.5 wt% each).

While the samples of the present study are generally richer in

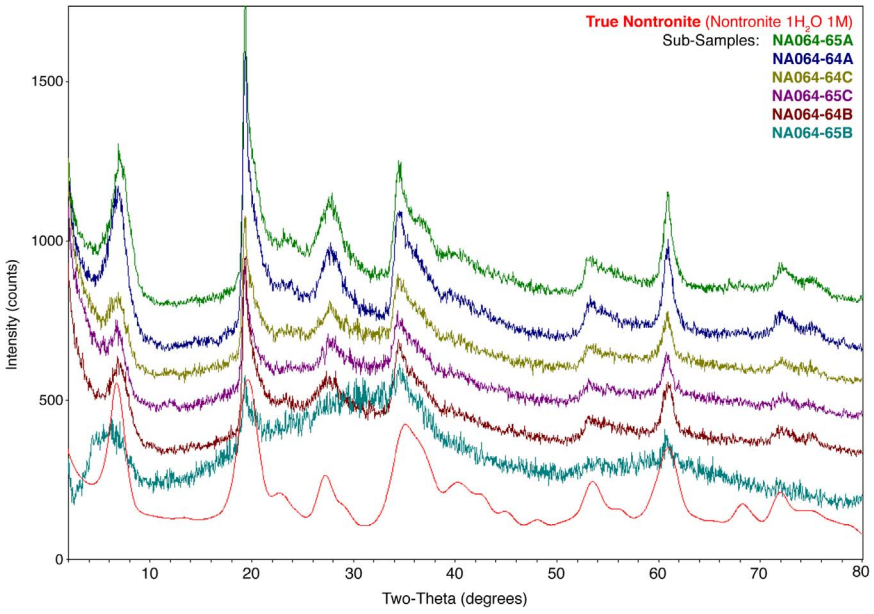

Fig. 5. X-ray diffraction patterns of sub-samples NA064-64A, NA064-64B, NA064-64C, NA064-65A, NA064-65B, and NA064-65C. Nontronite (Rietveld simulation, shown in solid red) is consistently observed throughout all sub-samples. The small peak at about 12° 2θ in NA064-65C is possibly a 7-Å Mn-oxide phase (birnessite group). Scans were run at 0.8°/minute (0.04°/step and 3 s/step). Patterns are offset on the y-axis (using a constant) for comparison purposes. (For interpretation of the references to color in this figure legend, the reader is referred to the web version of this article).

Fe_2O_3* compared to many other studies (Fig. 7; Table 2), the two green sub-samples (NA064-64A and NA064-65A) are geochemically similar to other nontronites (Fig. 7). Both NA064-64A and NA064-65A also have higher concentrations of MgO (Table 2) in comparison to hydrothermal deposits of Fe-oxides (Dekov et al., 2010; shown as larger circles numbered 16–20 in Fig. 7), which are geochemically most similar to the orange sub-samples of this study, NA064-64B and NA064-65B.

3.4. Trace elements

Trace element compositions for all six sub-samples and the two bulk samples are presented alongside data from 11 comparable studies (Table 3). Similar to hydrothermal nontronite samples, the deposits from Mashi contain generally low abundances of trace and rare earth elements. Samples from Mashi are most similar to those from hydrothermal mounds near the Galapagos Spreading Center (Hekinian et al., 1978) and Eolo Seamount (Dekov et al., 2007), with the exception of a noticeably lower concentration of Pb relative to Co (Fig. 8). Metal concentrations in hydrothermal smectites exhibit significant variability that has been attributed to the potential presence of amorphous metal-bearing sulfides, degree of subsurface fluid mixing, and the time of exposure to ambient water (DeCarlo et al., 1983).

There are relatively few studies of the complete rare earth element (REE) distribution patterns for hydrothermal nontronites (Severmann et al., 2004; Dekov et al., 2007). The chondrite-normalized REE patterns of the Mashi Seamount samples are all very similar in overall

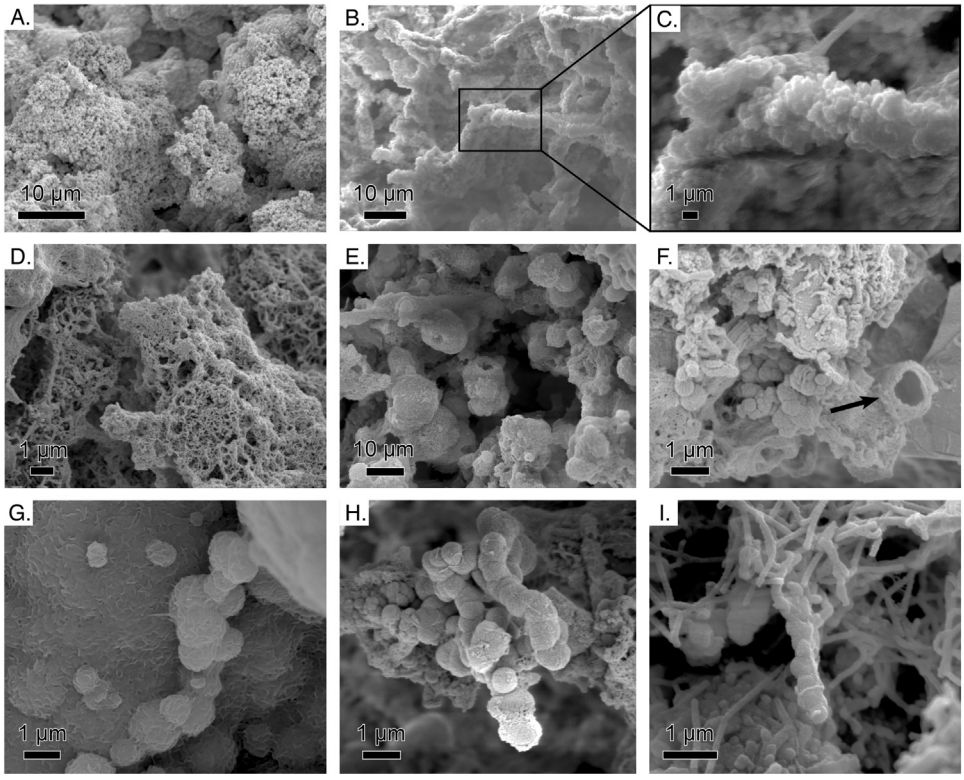

Fig. 6. Scanning electron micrographs. A. Specimen from sample NA064-64A; the sponge-like clay basic structure of the nontronite grains. B. Specimen from sample NA064-65A; hollow branching filamentous aggregates of nontronite with higher weight percentages of Si-oxides in comparison to Fe-oxides determined from EDS analyses. C. Close view of highlighted rectangle in B. Branches consist of characteristic fine clay sheets. D. Specimen from sample NA064-64B; web-like basic structures of Fe-oxides. E. Specimen from sample NA064-64B; hollow microspheres very rich in Fe-oxide (FeO), nearly 85 wt% indicated through EDS analysis. F. Specimen from sample NA064-64B; arrow points toward broken hollow filamentous aggregate. G. Specimen from sample NA064-65A; oblate microspheres of remnant microbial structures coated in fine overlapping clay sheets with relatively equal levels of Fe and Si oxides determined from EDS analyses. H. Specimen from sample NA064-64B; clusters of oblate microspheres. I. Specimen from sample NA064-64B; Fe-oxide filament structures with propagating oblate microspheres stemming off of the filaments.

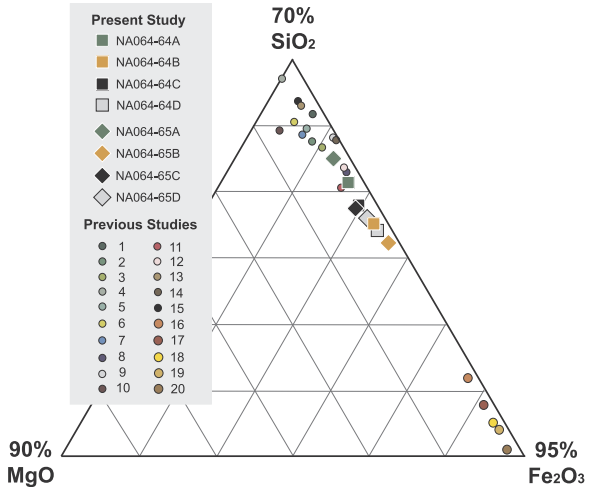

Fig. 7. Fe_2O_3 – MgO – SiO_2 ternary diagram of 28 samples, 20 from previous comparable studies and 8 from the present study are plotted as weight %. Diagram number references: 1 - Dekov et al. (2007), 2 - Alt et al. (1987), 3 - Murnane and Clague (1983), 4 - De Carlo et al. (1983), 5 - Corliss et al. (1978), 6 - Hekinian et al. (1978), 7 - Grill et al. (1981), 8 - Bischoff (1972), 9 - Cole (1988), 10 - Dymond and Eklund (1978), 11 - Hoffert et al. (1978), 12 - Dill et al. (1994), 13 - Stoffers et al. (1990), 14 - Severmann et al. (2004), 15 - McMurty et al. (1993), 16–20 – Dekov et al. (2010) (16: M78/2 335ROV-7, 17: M64/1 200ROV-5, 18: M64/1 200ROV-7, 19: M68/1 39ROV-1, and 20: M64/1 209GTV-a). (For interpretation of the references to color in this figure legend, the reader is referred to the web version of this article).

shape but exhibit different degrees of enrichment. Characteristic features include elevated La/Sm ratios (> 5), negative Ce and Eu anomalies, and elevated heavy REEs (Fig. 9). The shape of the trends and degrees of enrichment are very similar to those of the diffuse low temperature Fe-Si-oxyhydroxide deposits of the Lilliput hydrothermal field (from the Limtoc locale) on the mid-Atlantic ridge (Dekov et al., 2010). These patterns are virtually identical in shape and individual anomalies (Ce and Eu) to ambient seawater, although significantly enriched (Douville et al., 1999). In contrast, the Eolo Seamount nontronite pattern lacks a negative Ce anomaly and is overall more enriched relative to the Mashi samples (Fig. 9).

4. Discussion

4.1. Formation of the deposits

A combination of trace and major element data provides insights into the potential amorphous phases that are likely present in the different subsamples. Subsamples of the green clay (NA064-64A, NA064-65A), dark crustal material (NA064-64C, NA064-65C) and the bulk samples (NA064-64D, NA064-65D) define a somewhat linear trend on a plot of Fe_2O_3* versus V (Fig. 10) that could represent mixing between two dominant mineral end-members: one with low Fe_2O_3* and V, and one with high Fe_2O_3* and V. The low end, characterized by low Fe_2O_3* and V concentrations, is likely controlled by nontronite. A pure hydrothermal nontronite end-member could not be identified in the literature (due to mixing at hydrothermal sites), so a hypothetical nontronite end-member was constructed using the value of 24.7 wt% Fe_2O_3* (Brigatti, 1983) and assuming 0 ppm V. The high end of the mixing array, with high Fe_2O_3 and V, may be exemplified by poorly crystalline Fe-Si oxyhydroxides (e.g. Dekov et al., 2010), which are strongly enriched in both elements, in addition to Mn, Zn, and Co. According to this mixing plot, NA064-64A and NA064-65A contain about 45% nontronite and 10% Fe-Si oxyhydroxides whereas NA064-64C and NA064-65C contain 35% nontronite and 35% Fe-Si-oxyhdroxides. The higher content of V and Fe_2O_3* in the bulk samples (NA064-64D and NA064-65D) relative to the sub-samples suggests that the end-member with high V and Fe_2O_3*, interpreted here as Fe-Si oxyhydroxides, may have been preferentially excluded by the subsampling procedure. In contrast, the orange-red subsamples (NA064-64B, NA064-65B) fall off the potential mixing line and are characterized by low contents of V, Mn, and Zn at relatively high Fe_2O_3* (Fig. 10). These subsamples bear geochemical similarities to poorly crystalline disordered ferrihydrite (protoferrihydrite) phases that are associated with relatively low-temperature hydrothermal venting (e.g. Pichler and Veizer, 1999). Unlike the other Fe-Si oxyhydroxides, these phases contain high Fe, but low concentrations of metals such as V, Ni, and Mn, and are reddish-orange in color. A hypothetical mixing line between an average natural protoferrihydrite composition and the mixing array of the remaining samples suggests the B subsamples could represent mixtures containing 10% nontronite, 5% Fe-Si oxyhydroxide, and 85% protoferrihydrite. Based on this semi-quantitative analysis, it is clear that the green subsamples (NA064-64A, NA064-65A) fairly effectively excluded the Fe-Si oxyhydroxide component of the full sample but included ~50% protoferrihydrite. Overall, the orange subsamples (NA064-64B, NA064-65B) have preferentially concentrated the protoferrihydrite component. The dark crustal material (NA064-64C, NA064-65C) included a fairly equal mix of nontronite, Fe-Si oxyhydroxide, and protoferrihydrite. The bulk samples (NA064-64D, NA064-65D), however, included more Fe-Si oxyhydroxide than the orange (NA064-64B, NA064-65B) subsamples. It is important to note that these mixing proportions are only semi-quantitative and used to demonstrate general trends, but due to the assumptions used, they do not quantify exact proportions of the mineral phases present in each of the sub-samples.

X-ray diffraction patterns and geochemical data of samples from Mashi Seamount confirm the presence of nontronite mixed with poorly crystalline Fe-Si-oxyhydroxides and protoferrihydrite (Figs. 5, 9, and 10). These deposits are similar in their mineralogical and chemical composition to those sampled from other seamounts (Corliss et al., 1978; Hekinian et al., 1978; Grill et al., 1981; DeCarlo et al., 1983; Murnane and Clague, 1983; Alt et al., 1987; Dekov et al., 2007). Overall, the chemical consistency between samples from Mashi and those from other sites suggests that they are hydrothermal in origin and associated with low-temperature diffuse venting on the seafloor. Although no oxygen isotopic analyses were performed on the samples from Mashi, the presence of nontronite indicates formation temperatures between 20 °C and 80 °C based on results from other studies (DeCarlo et al., 1983; Murnane and Clague, 1983; Alt et al., 1987; Stoffers et al., 1990; McMurtry et al., 1993; Köhler et al., 1994; Severmann et al., 2004; Dekov et al., 2007).

Nontronite compositions published from a broad spectrum of seafloor geological environments (e.g. seamounts, ridges, hotspots) range from 46 to 57 wt% SiO_2 and 25–34 wt% Fe_2O_3* (Corliss et al., 1978; Hekinian et al., 1978; Grill et al., 1981; DeCarlo et al., 1983; Murnane and Clague, 1983; Alt et al., 1987; Dekov et al., 2007). In general, the nontronite compositions from Mashi Seamount are distinctly lower in SiO_2 and higher in Fe_2O_3* (Fig. 7). Higher Fe/Si ratios have been suggested as indicators of higher formation temperatures (> 40 °C; Murnane and Clague, 1983). The average Fe/Si ratios of samples in this study do appear to be higher than those documented in other studies (DeCarlo et al., 1983; Murnane and Clague, 1983; Alt et al., 1987; Stoffers et al., 1990; McMurtry et al., 1993; Severmann et al., 2004; Dekov et al., 2007), which could suggest that the formation temperatures were greater than 40 °C (Stoffers et al., 1990; McMurtry et al., 1993). Mixing constraints discussed above, however, suggest our subsampling methods did not capture a high-purity nontronite end-member and the higher Fe/Si ratios of the Mashi samples are the result of admixture of poorly crystalline Fe-Si oxyhydroxides with nontronite. Further evidence for a low temperature hydrothermal origin is provided by REE distribution patterns that show negative Ce and Eu anomalies similar to that of ambient seawater (Fig. 9). This indicates extensive dilution of hydrothermal fluids and dominance of the REE distribution pattern by that of seawater.

The process by which nontronite forms during low temperature

Table 2
Geochemical data for major elements of all eight sub-samples from NA064 (first eight columns; sample ID shorterned to the last three values, e.g. NA064-64A is shown as 64A) from the present study, in addition to sixteen comparable studies. All values presented in weight % and normalized to 100. References and sample identifications for comparable locations: 1. Dekov et al. (2007) – T/77-29 (113-5), 2. Alt et al. (1987) – 1183-14/15, 3. Murnane and Clague (1983) – TT152–11G, 4. De Carlo et al. (1983) – 20–2G, 5. Corliss et al. (1978) – N2, 6. Hekinian et al. (1978) – DSDP L54 bulk, 7. Grill et al. (1981) – 69-11-2, 8. Bischoff (1972) – average, 9. Cole (1988) – 10094 252–260, 10. Dymond and Eklund (1978) – average, 11. Hoffert et al. (1978) – average, 12. Dill et al. (1994) – RS 1, 13. Stoffers et al. (1990) – SO 35 KD80, 14. Severmann et al. (2004) – 2901-2, 15. McMurty et al. (1993) – S-8b, 16. Dekov et al. (2010) – M68/1 39ROV-7A.

Reference	Mashi Seamount, Galapagos Islands								Eolo Seamount[1]	Red Seamount[2]	Juan de Fuca Ridge[3]	Loihi Seamount[4]	Galapagos Rift[5]
	64A	64B	64C	64D	65A	65B	65C	65D					
SiO_2	48.81	42.55	44.67	41.53	52.43	40.12	44.57	42.68	55.74	54.42	52.80	61.39	57.04
Al_2O_3	0.25	0.28	0.20	0.22	0.05	0.09	0.10	0.08	5.31	0.01	0.36	2.94	0.04
Fe_2O_3	43.82	49.51	46.39	49.24	40.59	51.66	46.33	48.29	33.53	36.35	37.66	27.66	35.63
FeO	–	–	–	–	–	–	–	–	–	–	0.46	–	–
MnO	0.16	0.14	1.03	1.06	0.01	0.05	0.80	0.82	–	0.14	0.05	0.04	0.25
MgO	2.36	1.95	2.26	2.04	2.41	1.71	2.28	2.08	1.39	3.78	3.17	3.19	3.01
CaO	0.54	0.89	0.90	1.04	0.30	1.00	0.88	1.04	1.39	0.38	0.46	1.13	0.12
Na_2O	2.06	1.73	2.31	2.40	2.11	2.11	2.53	2.28	1.58	0.53	1.13	2.17	1.50
K_2O	1.31	1.11	1.05	1.10	1.84	1.28	1.41	1.34	1.06	4.39	3.85	0.66	2.41
P_2O_5	0.67	1.81	1.17	1.36	0.26	1.96	1.10	1.38	–	–	0.05	–	–
TiO_2	0.01	0.01	0.01	0.02	0.00	0.00	0.01	0.00	–	–	0.02	0.82	–
LOI	7.84	9.97	9.04	9.47	6.49	9.12	8.60	8.45	19.48	–	12.79	–	–
H_2O	4.68	9.08	7.39	5.00	8.42	10.72	7.92	8.76	–	–	–	–	–
Total	100	100	100	100	100	100	100	100	100	100	100	100	100

Reference	Galapagos Mounds[6]	Explorer Ridge[7]	Red Sea[8]	Red Sea[9]	Bauer Basin[10]	FAMOUS[11]	EPR 18°S[12]	Lau Basin[13]	TAG[14]	Kasuga 3 Seamount[15]	Limtoc at Lilliput[16]
SiO_2	56.39	54.29	47.98	55.04	55.45	44.65	52.07	60.75	56.67	58.65	9.56
Al_2O_3	0.39	1.86	3.21	0.42	2.59	0.27	0.06	0.24	0.34	0.78	0.05
Fe_2O_3	32.75	34.28	41.42	39.14	31.49	40.38	43.93	34.25	40.61	32.21	64.31
FeO	–	0.13	–	–	–	–	0.84	–	–	–	–
MnO	0.12	0.34	0.59	–	0.68	4.21	0.02	0.06	0.00	1.13	0.41
MgO	4.11	3.76	1.65	0.54	6.47	3.14	1.70	2.32	0.34	2.05	1.19
CaO	0.33	0.58	0.56	0.12	0.50	1.89	0.31	0.33	0.07	0.91	1.66
Na_2O	2.28	1.25	3.56	4.63	0.64	2.04	0.58	1.31	0.23	2.20	4.21
K_2O	3.60	3.36	1.03	0.12	2.16	3.41	0.24	0.64	1.14	1.63	0.18
P_2O_5	–	–	–	–	–	–	0.23	0.03	0.57	–	0.57
TiO_2	0.03	0.15	–	–	0.03	0.02	0.01	0.06	0.02	0.45	0.02
LOI	11.04	16.19	24.19	19.31	–	8.66	22.15	–	14.42	9.47	17.84
H_2O	–	–	–	–	–	–	–	–	–	–	–
Total	100	100	100	100	100	100	100	100	100	100	100

Table 3
Geochemical data for trace and REE of all eight sub-samples from NA064 (first eight columns; sample ID shorterned to the last three values) from the present study, in addition to eleven comparable studies. All values presented in ppm. References and sample identifications for comparable locations: 1. Dekov et al. (2007) – T/77-29 (113-5), 2. Alt et al. (1987) – 1183-14/15, 3. Murnane and Clague (1983) – TT152–11G, 4. De Carlo et al. (1983) – 20–2G, 5. Corliss et al. (1978) – N2, 6. Hekinian et al. (1978) – DSDP L54 bulk, 7. Hoffert et al. (1978) – average, 8. Dill et al. (1994) – RS 1, 9. Stoffers et al. (1990) – SO 35 KD80, 10. Severmann et al. (2004) – 2901-2, 11. Dekov et al. (2010) – M68/1 39ROV-7A.

Reference	Mashi Seamount, Galapagos Islands								Eolo Seamount[1]	Red Seamount[2]	Juan de Fuca Ridge[3]	Loihi Seamount[4]	Galapagos Rift[5]	Galapagos Mounds[6]	FAMOUS[7]	EPR 18°S[8]	Lau Basin[9]	TAG[10]	Limtoc at Lilliput[11]
	64A	64B	64C	64D	65A	65B	65C	65D											
Ag	–	–	–	–	–	–	–	–	0.01	–	–	–	–	–	–	–	–	–	–
As	37.74	60.45	48.73	62.20	8.06	37.93	45.24	60.14	351	2	–	12	2.9	–	–	12	–	–	–
Ba	101.97	89.94	119.77	118.77	6.77	29.63	90.64	67.28	22	38	130	–	68	–	73	39	< 10	–	39.9
Be	0.05	0.02	0.04	0.05	0.00	0.00	0.05	0.07	2.35	–	–	–	–	–	–	–	–	–	–
Bi	–	–	–	–	–	–	–	–	0	–	–	–	–	–	–	–	–	–	–
Cd	–	–	–	–	–	–	–	–	0.16	–	–	6.9	–	–	–	–	–	–	0.313
Co	0.66	0.58	1.54	1.75	0.08	0.08	1.10	1.93	1	1.6	1.13	43	0.91	22	5	< 7	< 10	–	14.3
Cr	3.17	3.32	2.74	3.90	0.00	0.05	3.76	3.95	5	2.7	4.8	45	4.1	11	9.5	< 7	33	–	–
Cs	0.55	0.43	0.39	0.56	1.10	0.60	0.61	0.81	1.5	3.3	4.8	–	–	–	–	–	–	–	< 0.09
Cu	2.61	3.57	3.78	3.69	0.28	0.54	5.24	7.34	5.3	330	23	89	8	14	67	–	48	–	8.38
Ga	0.41	0.16	0.32	0.25	0.02	0.03	0.15	0.19	1	–	–	–	–	–	5	–	–	–	–
Ge	–	–	–	–	–	–	–	–	2.02	–	–	–	–	–	–	–	–	–	–
Hf	0.06	0.03	0.04	0.06	0.01	0.01	0.06	0.05	< 5	0.05	0.12	–	–	–	–	–	–	–	< 0.06
In	–	–	–	–	–	–	–	–	0.003	–	–	–	–	–	–	–	–	–	–
Li	2.40	2.12	9.06	9.50	1.34	1.78	7.35	7.87	2	–	–	1	–	–	–	–	–	–	5.85
Mo	–	–	–	–	–	–	–	–	28	–	–	–	–	–	–	–	–	–	83.6
Nb	0.14	0.09	0.13	0.15	0.00	0.01	0.10	0.13	0.9	–	–	–	–	–	–	–	–	–	0.019
Ni	4.16	2.56	15.08	15.50	0.76	0.89	14.14	34.44	3	< 45	–	118	14	16	49	< 7	< 10	–	4.04
La	2.74	2.71	2.44	3.14	1.70	2.07	1.49	2.64	2.7	0.17	2.01	–	2.2	–	–	–	–	0.46	0.185
Ce	1.14	1.34	1.12	1.17	0.48	0.75	0.44	0.90	6.3	0.22	4.17	–	2.3	–	–	< 15	–	0.58	0.089
Pr	0.32	0.39	0.34	0.34	0.14	0.22	0.18	0.33	0.9	–	–	–	–	–	–	–	–	0.06	0.027
Nd	1.49	1.78	1.55	1.58	0.65	1.05	0.82	1.54	4	< 3	–	–	–	–	–	–	–	0.26	0.127
Sm	0.28	0.33	0.29	0.29	0.11	0.17	0.16	0.29	1	0.05	0.71	–	0.49	–	–	–	–	0.07	0.035
Eu	0.09	0.10	0.09	0.10	0.03	0.05	0.05	0.09	0.24	0.01	0.19	–	0.15	–	–	–	–	0.11	0.011
Gd	0.47	0.51	0.48	0.53	0.20	0.30	0.28	0.50	1.1	–	–	–	–	–	–	–	–	0.05	0.042
Tb	0.07	0.08	0.08	0.08	0.03	0.04	0.05	0.08	0.19	< 0.02	0.15	–	–	–	–	–	–	0.01	0.007
Dy	0.55	0.59	0.55	0.63	0.21	0.34	0.37	0.60	1.5	–	–	–	–	–	–	–	–	0.05	0.051
Ho	0.16	0.16	0.15	0.19	0.06	0.10	0.11	0.17	0.36	–	–	–	–	–	–	–	–	0.01	0.014
Er	0.51	0.52	0.49	0.62	0.19	0.34	0.36	0.57	1.27	–	–	–	–	–	–	–	–	0.03	0.047
Tm	–	–	–	–	–	–	–	–	0.23	–	–	–	–	–	–	–	–	0.00	0.008
Yb	0.52	0.51	0.49	0.63	0.17	0.32	0.39	0.60	1.65	0.02	0.56	–	0.30	–	–	–	–	0.03	0.051
Lu	0.09	0.09	0.08	0.11	0.03	0.06	0.07	0.11	0.28	0.08	0.10	–	0.03	–	–	–	–	0.00	0.01
Pb	0.40	0.44	0.50	0.50	0.03	0.21	0.44	1.10	3.9	80	–	340	–	60	–	135	< 5	–	< 0.32
Rb	20.25	16.11	15.37	18.34	33.04	19.53	19.34	20.57	11	125	111	–	–	–	–	17	21	–	0.6
Sb	0.86	1.26	1.53	1.75	0.38	0.93	1.40	2.42	0.38	2	3.05	–	0.9	–	–	–	–	–	4.31
Sc	0.43	0.27	0.82	0.64	0.01	0.03	1.15	0.34	1	0.36	0.7	–	0.19	–	–	–	–	–	< 1.51
Se	0.03	0.03	0.06	0.06	0.01	0.02	0.06	0.08	0.1	–	–	–	–	–	–	< 3	–	–	–
Sn	–	–	–	–	–	–	–	–	–	–	–	–	–	–	–	–	–	–	< 1.77
Sr	128.35	223.71	213.96	265.06	69.47	271.84	237.02	268.88	71	–	50	–	–	–	223	14	66	–	479
Ta	0.00	0.00	0.00	0.01	0.00	0.00	0.00	0.00	0.06	0.02	0.05	–	–	–	–	–	–	–	< 0.46
Th	0.03	0.02	0.02	0.02	0.01	0.00	0.03	0.02	0.6	0.08	0.18	–	–	–	–	–	–	–	< 0.07
Tl	–	–	–	–	–	–	–	–	0.064	–	–	–	–	–	–	–	–	–	0.51
U	0.33	0.21	0.63	1.03	0.25	0.19	0.73	1.33	0.62	< 0.15	0.16	–	–	–	–	16	–	–	10.5
V	42.24	22.30	58.92	74.71	3.24	3.57	68.72	103.82	18	–	–	–	–	–	94	22	45	–	63.9
W	–	–	–	–	–	–	–	–	7	–	–	–	–	–	–	16	–	–	0.68
Y	8.17	8.11	7.20	10.59	3.43	6.80	6.61	9.06	7.1	–	–	–	–	–	–	–	–	–	1.21
Zn	29.45	22.62	39.73	45.24	15.29	12.09	33.40	62.52	9	670	136	640	29	35	14	–	43	–	37.7
Zr	3.68	2.08	3.24	3.75	0.30	0.34	4.04	4.71	13	–	–	–	–	–	–	< 7	–	–	< 2.13

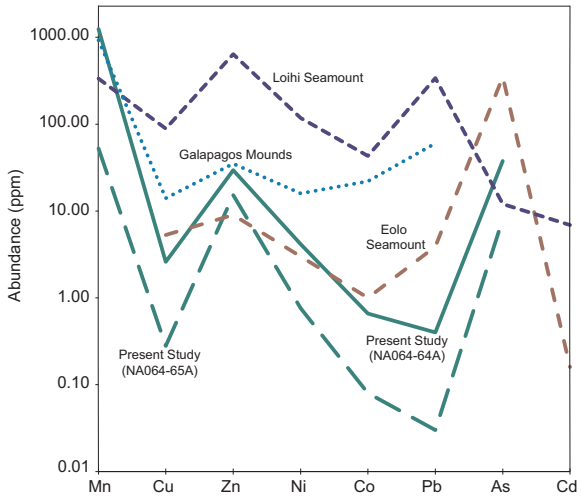

Fig. 8. Comparative trace element plot of several submarine nontronites. Nontronites from the present study are displayed as a solid green line and a long-dashed green line for samples NA064-64A and NA064-65A, respectively. Eolo Seamount data (Dekov et al., 2007) displayed as a red medium-dashed line; Loihi Seamount data (De Carlo et al., 1983) displayed as a dark blue short-dashed line; Galapagos Mounds data (Hekinian et al., 1978) displayed as a light-blue dotted line. (For interpretation of the references to color in this figure legend, the reader is referred to the web version of this article).

hydrothermal venting has been the subject of considerable speculation. One hypothesis is that simple abiotic precipitation occurs from Fe-rich fluids in areas of strong oxidation-reduction gradients (Murname and Clague, 1983; DeCarlo et al., 1983). For nontronite to form by abiogenic precipitation, the presence of reduced iron (Fe^{2+}) in the upwelling hydrothermal fluids is essential because it helps stabilize and control the formation of the nontronite octahedral layer (Harder, 1978). The redox potential (Eh) must also remain below zero in order to maintain some ferrous iron for nontronite formation and avoid oxidizing all of the Fe^{2+} and the precipitation of (proto)ferrihydrite instead of nontronite (Jambor and Dutrizac, 1998). The general temperature conditions are also very specific for seafloor hydrothermal nontronite formation. Nontronite typically will not form outside of the temperature range of 15–96 °C (Dekov et al., 2007); at higher temperature systems (e.g. high-temperature channelized vents), Fe-oxyhydroxides will typically form instead (DeCarlo et al., 1983).

More recent studies have emphasized the potential role of microbes in facilitating nontronite precipitation (e.g. Alt, 1988; Köhler et al., 1994; Ueshima and Tazaki, 2001; Dekov et al., 2007; Dekov et al., 2010). This has been driven largely by the discovery of remnant microbial structures in the deposits, such as filaments, globular aggregates, oblate microspheres, and elongate tubes (e.g. Li et al., 2012). One biologically-facilitated process suggested by Dekov et al. (2007) is that nontronite forms by aging and transformation of poorly-ordered Fe-Si oxyhydroxides that coat filaments of Fe-oxidizing bacteria (FeOB). These bacteria are known to play a major role in the precipitation of oxidized iron from a wide range of hydrothermal systems (Emerson and Moyer, 2002; Emerson et al., 2010). The degree of acidity (pH) is a critical parameter in controlling the kinetics of Fe^{2+} oxidation, and under high acidity (low pH) conditions microbial-activated precipitation of Fe-oxyhydroxides is enhanced compared to the much slower rates of abiotic oxidation (Ferris, 2005). Alternatively, Ueshima and Tazaki (2001) presented an experimental model for direct biogenic formation of nontronite through microbial polysaccharides. They observed that specific bacteria are able to secrete extracellular polymer substrates (EPS) in order to protect themselves from severe environmental conditions. This EPS acts as a biofilm and a reactive geochemical surface. Nontronite formation occurs within the EPS on top of bacterial cells while Fe-Si oxyhydroxides form outside of the EPS. Although they investigated this phenomenon on polysaccharide EPS, EPS can consist of lipids, proteins, and other types of organic compounds (Fortin et al., 1998; Ueshima and Tazaki, 2001). The precipitation time for nontronite is generally very slow and there must be a framework such as that provided by EPS where a 'template' is offered to orient the required tetrahedral silicate sheet (e.g. polysaccharide) onto the polymers of the EPS (Ueshima and Tazaki, 2001).

SEM images from Mashi samples reveal structures that are similar to the morphology of documented bacterial structures observed in other nontronite-bearing deposits (e.g. Köhler et al., 1994; Ueshima and Tazaki, 2001; Dekov et al., 2007; Dekov et al., 2010; Li et al., 2012). In particular, globular aggregates, oblate microspheres, and filamentous structures (Fig. 6) are similar to those shown in Li et al. (2012) as well as the thread-like bacterial structures encrusted in Fe-sulfides from Dekov et al. (2010). Microspheres from Mashi samples appear to have a central hole where an abandoned bacterium (Fig. 6E) likely once resided, with high iron (Fe-Si oxyhydroxide and/or protoferrihydrite) material surrounding it as determined by EDS analysis. A specimen from NA064-64B also shows broken hollow filaments that were perhaps vacated by bacteria (Fig. 6F). SEM imagery from the nontronite subsample NA064-65A reveals several microspheres with a filmy layered surface texture (Fig. 6G) which is similar to those observed on the young cocci or bacilli microbes during experimental growth of nontronite (Ueshima and Tazaki, 2001). This kind of textured surface may also suggest an early stage of the characteristic honeycomb precipitates of nontronite aggregates (Eushima and Tazaki, 2001; Dekov et al., 2007). These spheres are also similar in size to those from Eushima and Tazaki's (2001) experiments at around 1 μm. Without the central indent (where potential microbes vacate), these likely younger structures may still have contained microbes.

These micro-morphologies are perhaps the best evidence for microbially-mediated precipitation of at least the Fe-Si oxyhydroxide

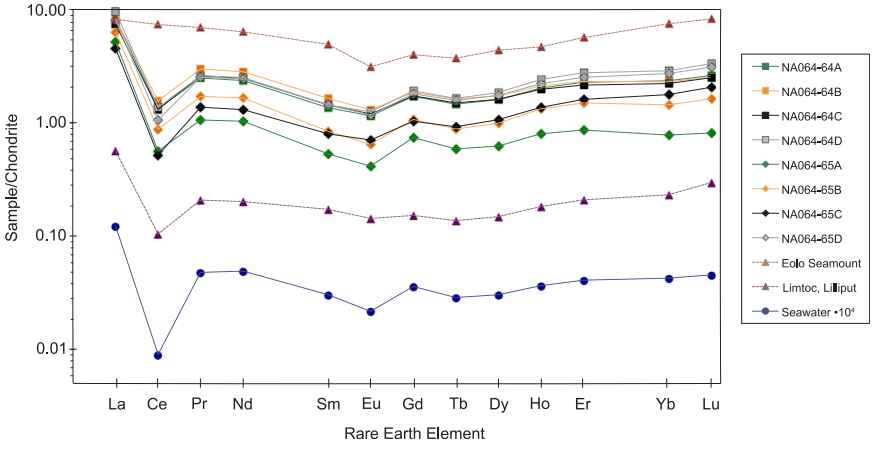

Fig. 9. REE distribution patterns normalized to CI chondrite (Sun and McDonough, 1989). Comparative REE patterns are presented for the Eolo Seamount nontronite (T/77-29 (113 – 115); Dekov et al., 2007) and the amorphous Fe-Si oxyhydroxides from the Limtoc site at Lilliput Hydrothermal Field (M68/1 39ROV-7A; Dekov et al., 2010). The closed blue triangles refer to REE data of seawater (Atlantic deep seawater, TAG 3300 m; Douville et al., 1999) multiplied by a factor of 10^4 for comparison purposes. (For interpretation of the references to color in this figure legend, the reader is referred to the web version of this article).

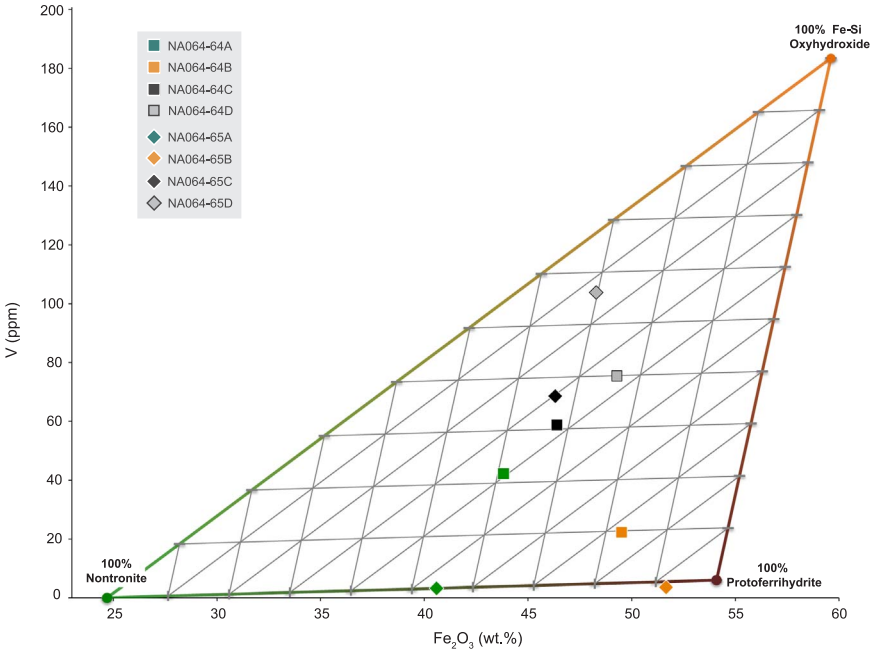

Fig. 10. Plot of Fe_2O_3 versus V showing the mixing relationships between subsamples of this study with three prominent end-members (nontronite, Fe-Si oxyhydroxide, and protoferrihydrite). The nontronite end-member was constructed using the literature value of 24.7 wt% Fe_2O_3* (Brigatti, 1983) and 0 ppm V. The Fe-Si oxyhydroxide end-member value represents an average two Fe-Si oxyhydroxide samples (M64/1 200ROV-5 and M64/1 200ROV-5) from the Lilliput hydrothermal field, which contained the highest Fe_2O_3 and V (Dekov et al., 2010). The protoferrihydrite end-member is from sample V-2B II, a protoferrihydrite precipitate from Tutum Bay, Ambitle Island, which contained the highest Fe content identified in previous studies (Pichler and Veizer, 1999).

phases of the Mashi deposits. The surface appearance of most of the observed microstructures does not have a well-defined honeycomb exterior like that observed for freshly precipitated nontronite (Köhler et al., 1994; Ueshima and Tazaki, 2001). However, the microstructures observed in the Mashi samples do look similar to some of the Fe-Si oxyhydroxides presented in Dekov et al. (2010) and Li et al. (2012). With such high SiO_2 contents in the samples from Mashi, it is clear that some of the microstructures observed are Si-oxyhydroxides, not just Fe-oxides and nontronite. Perhaps this may explain some of the discrepancies in appearance with those of pure natural nontronite and young (experimentally precipitated) nontronite (Ueshima and Tazaki, 2001). It is unclear from the available evidence whether the nontronite from the Mashi samples formed through an aging of precursor Fe-oxyhydroxides or if it was precipitated directly within EPS of microbes. However, the abundance of remnant bacterial structures clearly points to an important role of biologically mediated processes during formation of these deposits. This is also supported by the occurrence of soft, orange-yellow microbial mats, indicative of Fe-oxidizing bacteria (Dave Emerson, personal communication), in cracks and crevices of the nontronite-bearing tubes on Mashi Seamount (Fig. 3B).

4.2. Origin of the tubular distribution pattern

To our knowledge, the tube-shaped sinuous pattern of hydrothermal deposits at Mashi Seamount has never been documented before. The highly regular pattern of the tubes suggests that some similarly regular structure or feature beneath the deposit may have controlled the fluid flow. Pillow lavas are common formations on and around seamounts, and were observed along the ROV transect up the slopes onto the summit of Mashi. It appears that the spatial scales of the roughly circular areas defined by the nontronite tubes (Fig. 3) are similar to the size of individual pillows lobes in nearby lava flow outcrops (Fig. 11). We suggest that spaces between pillows may have been locations with enhanced fluid flow and that the deposits grew in response to this constrained flow pattern. In order to examine this hypothesis, image analysis was performed on ROV bottom photographs of the tubular deposits on Mashi as well as nearby pillow lava outcrops (see methods for details; Fig. 11). There is a clear similarity between the spatial dimensions of the nontronite areas and individual pillow lobes (Fig. 12), suggesting that the tubular distribution is likely controlled by an underlying lava flow formation. Additional evidence for this relationship was discovered in ROV imagery at the edge of the nontronite field where the tubular deposits feathered out and revealed underlying outcrops of pillow lava (Fig. 11C).

We propose that the nontronite deposits at Mashi Seamount represent a diffuse flow hydrothermal vent system on an underlying pillow lava sequence and here present a model for its development and evolution (Fig. 13). The first phase begins with eruption and emplacement of a fresh pillow lava formation (Fig. 13A). In the second phase, seawater infiltrates the lava sequence and establishes preferential flow through cracks and spaces between individual pillow lobes. Sediment begins to accumulate on the pillow lava surface, but diffuse flow continues to vent through pathways between pillows (Fig. 13B). As time passes, continued pelagic sedimentation buries the surface of the pillow lava and diffuse fluid is channelized along the low points between pillow lobes. The hydrothermal fluids may be denser than ambient seawater due to phase separation at depth (Bischoff and Rosenbauer, 1987) and thus tend to form horizontally-orientated (and in this case, tubular) deposits rather than vertical chimneys. It is also possible that the fluid flow is so minimal that vigorous plumes are not generated and fluids just seep out along cracks and mix with seawater quickly. Mineral precipitation of Fe-Si oxyhydroxides, protoferrihydrite, and nontronite from the low temperature fluids builds tubes or horizontal “chimneys” in between the pillow lobes (Fig. 13C). A distinctive feature of the tubes is the strong zonation of color and mineral phases from the interior (dominantly green nontronite) through bright orange (Fe-oxyhydroxides/nontronite mixtures) (Fig. 4) to a darker external crust (some manganese oxide) with yellowish microbial mats on the exterior (Fig. 3B). Similar zonations from other nontronite-bearing deposits have been attributed to development of mineral phases along significant oxidation-reduction gradients with more reducing fluids on the interiors of the tubes grading outward towards more oxygen-rich ambient seawater (DeCarlo et al., 1983). We suggest that the oxidation-reduction gradients may provide the necessary environments for biologically mediated growth of the observed mineral zonations. Fe-oxidizing bacteria need oxygen to survive, so they colonize the outermost parts of the tubes where there is access to well-oxygenated seawater (Figs. 3B and 4B). These bacteria produce loosely ordered Fe- and Si-oxyhydroxides over bacterial filaments, and the colonization front moves outward to stay in contact with an oxidizing environment. The Fe-Si oxyhydroxide byproducts eventually age within the tubes and undergo conversion to nontronite in a more reducing environment as

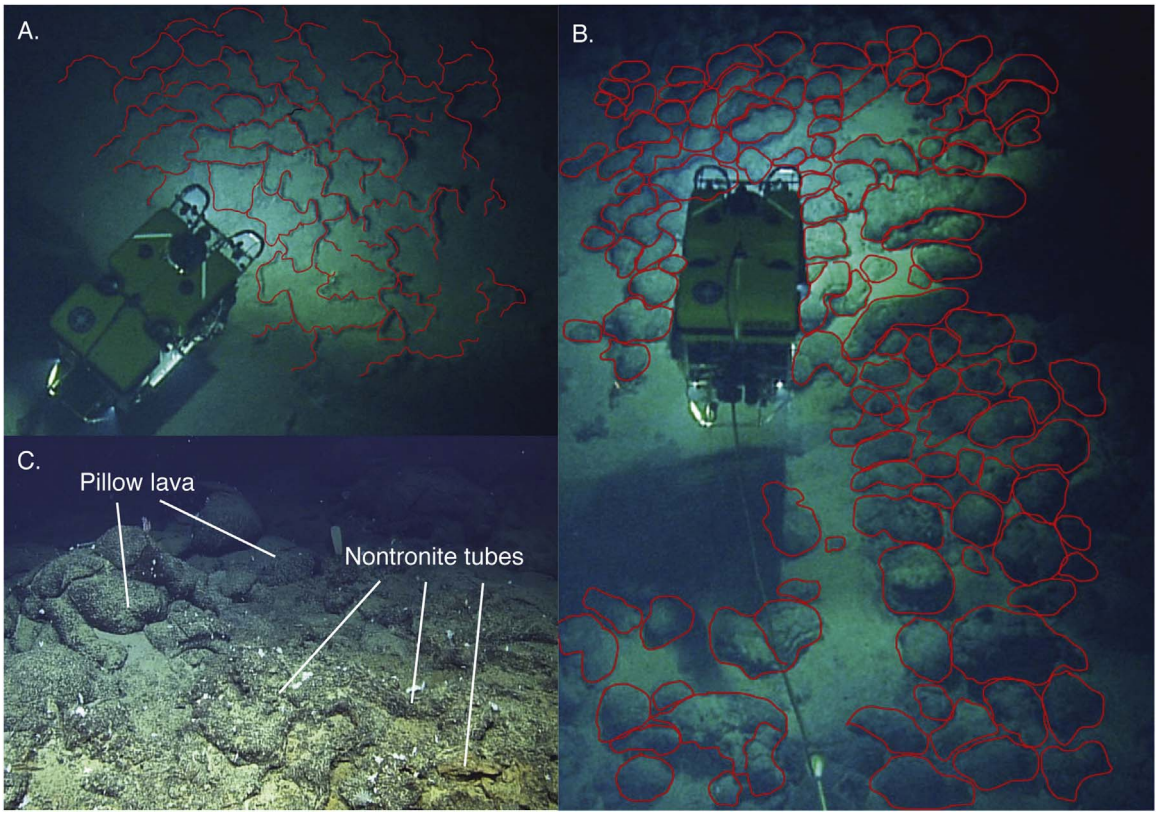

Fig. 11. A. Tracings (red) of the tubular nontronite-bearing deposits on Mashi Seamount as viewed from ROV *Argus*. ROV *Hercules*, 1.73 m wide and 3.86 m long (for scale), is shown in lower left side of the image. B. Tracings (red) of the individual pillow lava lobes as viewed from *Argus*. *Hercules* is shown in the upper left side of the image. C. Image showing the boundary of the nontronite-bearing tubular deposit with exposures of underlying pillow lava lobes. (For interpretation of the references to color in this figure legend, the reader is referred to the web version of this article).

proposed by Dekov et al. (2007).

In the latter stages of the hydrothermal system, as the heat source continues to diminish, sedimentation eventually evens out the original irregular pillow lava surface, but low volume fluid flow continues to feed the network of tubes (Fig. 13D). Fluid flow is extremely minor at this point but still sufficient to maintain active colonies of Fe-oxidizing bacteria. This is the current state of the Mashi Seamount system and is interpreted to represent the waning stages of the hydrothermal activity. It is anticipated that the sinuous tubes would eventually become completely buried by sedimentation and become recognized only as a metalliferous sediment zone overlying the pillow lava sequence.

4.3. Significance of nontronite-bearing diffuse venting systems

The common occurrence of nontronite deposits on the summits of many young oceanic seamounts indicates that the presence of diffuse flow hydrothermal systems is an integral part of a seamount's geochemical evolution and maturation. Our study demonstrates that deposits from such systems can have complex three-dimensionality to their distribution that may only be observable for a finite time before burial and incorporation into the sediment cover as a seamount becomes inactive. Dekov et al. (2007) point out that the lack of nontronite in ancient metalliferous sequences is evidence that transformations to other phases such as kaolinite-like amorphous aluminosilicates, poorly crystalline Fe-oxyhydroxides, and silica may occur by alteration under a variety of conditions. They also suggest that the impact of nontronite formation on seawater chemistry is not significant as the mineral does not act as a major sink for trace and REE elements from seawater (Figs. 8 and 10).

The presence of low-temperature, nontronite-bearing hydrothermal systems on seamounts may provide evidence for the potential of more extensive subsurface mineralization zones involving sulfides. Previous studies of diffuse hydrothermal venting with deposition of Fe-oxyhydroxides and nontronite have demonstrated that subsurface sulfide mineralization can occur in close proximity to the seafloor. For example, at Palinuro seamount in the Tyrrhenian Sea, massive sulfide deposits were found only tens of centimeters below seafloor venting that produced Fe-oxyhydroxide and nontronite chimneys (Petersen et al., 2008; Monecke et al., 2009).

5. Conclusions

Remotely operated vehicle (ROV) exploration of Mashi seamount in the Galapagos Islands discovered an unusual tubular hydrothermal deposit near the summit at 1227 m water depth. The porous and friable tubes exhibit a strong zonation in color and mineral phases with an interior dominated by bright green nontronite grading outwards to mixtures of nontronite, Fe-Si oxhydroxides, protoferrihydrite, and ending with a more indurated Mn-oxide crust topped with yellowish microbial flock. Major and trace element analyses of the deposits are similar to other nontronite-bearing deposits from hydrothermal vent systems at seamounts and spreading centers, but in general tend to have slightly higher Fe_2O_3* contents. Higher iron values likely represent admixture of nontronite with other poorly crystalline Fe-Si oxyhydroxide and protoferrihydrite phases. REE element distribution patterns exhibit high La/Sm ratios (> 5), negative Ce and Eu anomalies, and elevated heavy REE abundances. These patterns mimic that of seawater and indicate that the nontronite was likely derived from low temperature diffuse hydrothermal venting at the seamount. We propose that precipitation of mineral phases was facilitated by chemosynthetic microbes as shown by the presence of remnant structures such as filaments, microspheres, and hollow tubes revealed by SEM imaging. Fe-

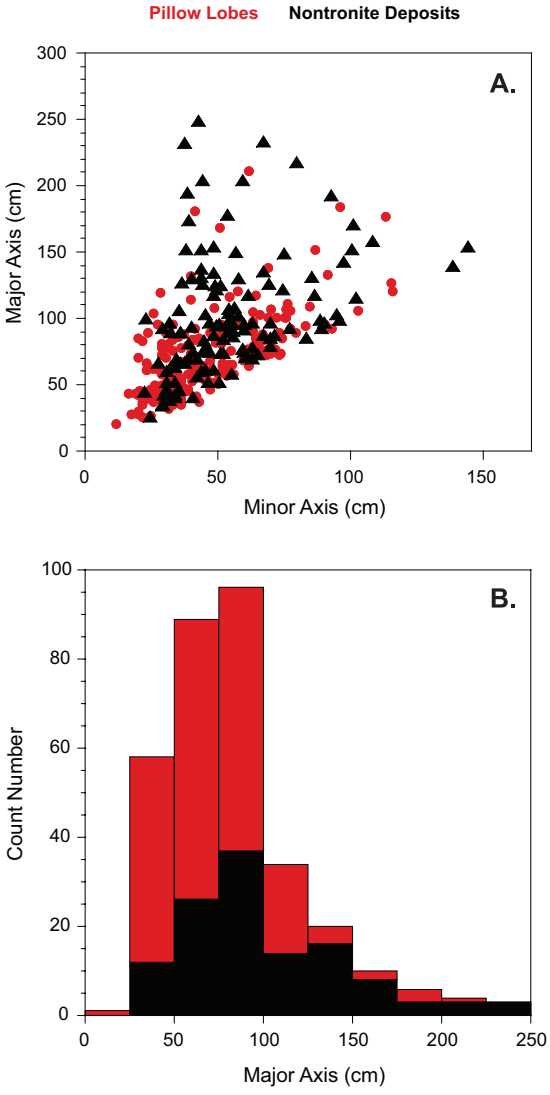

Fig. 12. A. Comparison of the major and minor axis dimensions of each of the traced outlines of both pillow lobes (red dots) and nontronite deposits (black triangles) on Mashi Seamount (see Fig. 9 for examples of these traced outlines). B. Histogram showing the distribution of longer (major) axis measurements for pillow lobes (red) and nontronite deposits (black). (For interpretation of the references to color in this figure legend, the reader is referred to the web version of this article).

oxidizing bacteria may have created precursor Fe-Si oxyhydroxides along the oxygen-rich tube exteriors. These phases transformed with time into nontronite that became the interior phase as the bacteria continually migrated outward to maintain their position in an oxidizing environment.

Based on quantitative analysis of images from the nontronite deposits and associated pillow lava outcrops, the unusual tubular distribution pattern is attributed to the preferential development of diffuse flow through cracks and spaces between individual pillow lobes in an underlying lava flow sequence. Evidence for this includes 1) a strong similarity between the spatial scales of the areas bounded by the tubes and the dimensions of individual pillow lobes, and 2) observations at the margins of the hydrothermal deposits where an underlying pillow lava sequence is exposed at the surface.

Acknowledgements

We gratefully acknowledge the Ocean Exploration Trust as well as the pilots and crew aboard the E/V *Nautilus* during cruise NA064 for their assistance in sample collection and exploration on Mashi Seamount, as well as NOAA grant NA15OAR0110220, which funded the shiptime. We acknowledge the NSF Grant OCE1258771 for support of curatorial activities on samples from cruise NA064. Further acknowledgements and thanks go out to the Charles Darwin Research Station and the Galapagos National Park Directorate for their collaboration and assistance in the exploration of the Galapagos Platform conducted under research permit No. PC-45-15. We also gratefully recognize the Government of Ecuador via the Ecuadorian Navy for permission to operate in their territorial waters. Major thanks and acknowledgments to the Bates College Student Research Fund and the Bates College Geology Department for both financial support and for the invaluable senior thesis experience which made this publication possible. Additional thanks go to David Emerson for the guidance regarding the various analyses involving FeOB, and to Gregory Anderson for the SEM-EDS technical support. We also extend thanks to two anonymous reviewers for their comments and suggestions that helped improve this manuscript. This publication is contribution number 2180 of the Charles Darwin Foundation for the Galapagos Islands.

Appendix A. Detailed methodology

X-ray diffraction

The six sub-samples were crushed as described in the materials and methods section. The resulting powders consisted of fine grain sizes appropriate for powder X-ray diffraction in the Rigaku Miniflex diffraction system. Powder diffraction mounts were prepared for each of the six samples. A flat piece of glass was pressed evenly over the surface of the mount to produce a consistent plane for X-ray diffraction measurement. All six mounts were placed in a six-position auto-sampler. Diffracted X-rays were detected by the machine at several different angles. D-values and percent composition of the sample were derived from this data. This derivation was completed using Bragg's Law.

Inductively coupled plasma mass spectrometry

The chemical composition of the samples was determined by inductively coupled plasma mass spectrometry (ICP-MS) for rare earth elements (REE), trace elements, and for P_2O_5 and K_2O. ICP-MS is very fast, more precise, and much more sensitive than ICP-AES. ICP-MS can measure one part per quadrillion so it is an excellent tool for trace and rare earths that may be present at very small concentrations.

Sample preparation for ICP-MS analysis involved dissolution of powdered samples in HF-HNO_3 acid digestion (methodology from Kelley et al., 2003) and was performed by Katherine Kelley at the University of Rhode Island Graduate School of Oceanography. In this methodology, 0.05 g of powdered sample (crushed and powdered with a mixer mill) is measured and placed into 23 ml Savillex Teflon beakers. 3 ml of 8NHNO_3 and 1 ml of HF are added to the powdered samples in each beaker. Samples are digested and evaporated to dryness overnight on a hot plate at 90 °C. These digested and dried samples are dissolved back into 3 ml of 8NHNO_3 and 3 ml of deionized water. Then they are diluted with deionized water to 2000x the original powder weight within HDPE bottles and sonicated for a duration of 30 min. Kelley et al.'s (2003) methodology is very effective at minimizes molecular interferences because it does not include HCl and $HClO_4$ as some ICP-MS methods do.

Inductively coupled plasma atomic emission spectroscopy

Major elemental compositions for SiO_2, MnO, Fe_2O_3, MgO, TiO_2, CaO, Al_2O_3, and Na_2O were determined by inductively coupled plasma atomic emission spectroscopy (ICP-AES). ICP-AES is less precise and less sensitive in comparison to the ICP-MS. For this reason, it is more suitable for measuring compositions of major oxides present in the samples.

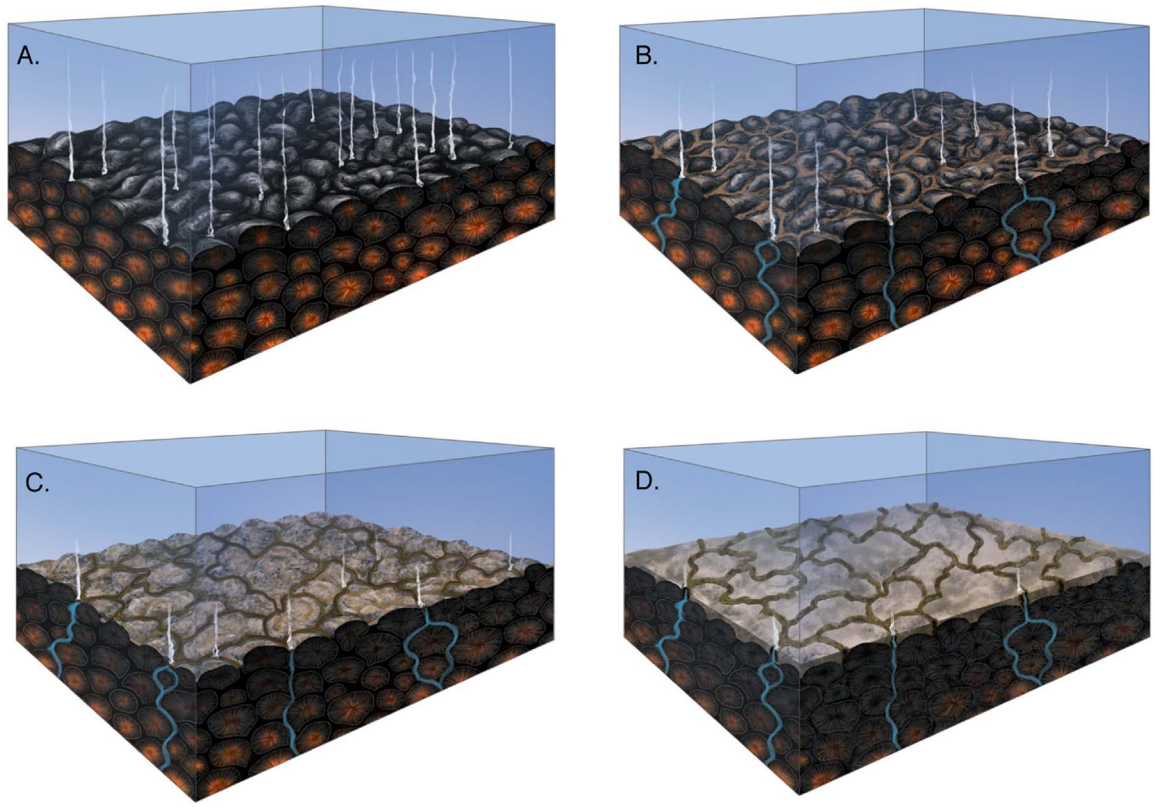

Fig. 13. Model for the development and evolution of the Mashi Seamount tubular hydrothermal deposits. A. Initial emplacement of pillow lava flow on seafloor with seawater infiltration and heating. B. Partial sedimentation and fluid flow directed through crack/spaces between pillow lobes. C. Continued sedimentation of pillow lobes and development of tubular hydrothermal deposits in areas of fluid flow. D. Burial of pillow lobes with waning hydrothermal venting and subdued growth of tubular deposits.

Sample preparation for ICP-AES analysis also followed the methodology from Kelley et al. (2003) and was performed by Katherine Kelley at the University of Rhode Island. In this procedure, solutions are prepared using $LiBO_2$ flux-fusions (Klein et al., 1991). 0.2 g of each sample is powdered and dried in Al crucibles within a 100 °C muffle furnace. The dry weight is recorded after one hour. Then crucibles are heated to 950 °C in a muffle furnace. After 45 min they are weighed again. These weights are used to measure the mass loss on ignition (LOI). 0.1 g of the ignited powder is measured and placed in new crucibles (high-purity graphite). Within these crucibles is 0.4 g of $LiBO_2$ flux, which mixes with the sample. Crucibles are placed into a muffle furnace at 1050 °C for 15 min. HDPE bottles are prepared and filled with 50 ml of 5% HNO_3. Molten beads from the crucibles are poured into HDPE bottles and shaken until fully dissolved. Clean HDPE bottles are prepared and contain 70 ml of 5% HNO_3. 10 ml of solution for each sample is pulled up and ejected out of syringes through 0.45 mm filters into these HDPE bottles. These new solutions are diluted at about 860x the total weight of the solids and 4300x the original sample weight.

References

Alt, J.C., Lonsdale, P., Haymon, R., Muehlenbachs, K., 1987. Hydrothermal Sulfide and Oxide Deposits on Seamounts Near 21°N 98. Geological Society of America, East Pacific Rise, pp. 157–168.

Alt, J.C., 1988. Hydrothermal oxide and nontronite deposits on seamounts in the eastern pacific. Mar. Geol. 81, 227–239.

Behn, M.D., Conrad, C.P., Silver, P.G., 2004. Detection of upper mantle flow associated with the African superplume. Earth Planet. Sci. Lett. 224, 259–274.

Bemis, K., Lowell, R.P., Farough, A., 2012. Diffuse flow on and around hydrothermal vents at mid-ocean ridges. Oceanography 25 (1), 182–191. http://dx.doi.org/10.5670/oceanog.2012.16.

Bischoff, J.L., 1972. A ferroan nontronite from the Red Sea Geothermal System. Clays Clay Miner. 20, 217–223.

Bischoff, J., Rosenbauer, R.J., 1987. Phase separation in seafloor geothermal systems: an experimental study of the effects on metal transport. Am. J. Sci. 287, 953–978.

Brigatti, M.F., 1983. Relationships between composition and structure in Fe-rich smectites. Clay Miner. 18, 177–186.

Cole, T.G., 1988. The nature and origin of smectite in the Atlantis II Deep, Red Sea. Can. Mineral. 26 (4), 755–763.

Corliss, J.B., Lyle, M., Dymond, J., Crane, K., 1978. The chemistry of hydrothermal mounds near the Galapagos Rift. Earth Planet. Sci. Lett. 40, 12–24.

DeCarlo, E.H., McMurtry, G.M., Yeh, H.W., 1983. Geochemistry of hydrothermal deposits from Loihi submarine volcano, Hawaii. Earth Planet. Sci. Lett. 66, 438–449.

Dekov, V.M., Kamenov, G.D., Stummeyer, J., Thiry, M., Savelli, C., Shanks, W.C., Fortin, D., Kuzmann, E., Vertes, A., 2007. Hydrothermal nontronite formation at Eolo Seamount (Aeolian volcanic arc, Tyrrhenian Sea). Chem. Geol. 245, 103–119.

Dekov, V.M., Petersen, S., Garbe-Schonberg, C.D., Kamenov, G.D., Perner, M., Kuzmann, E., Schmidt, M., 2010. Fe-Si-oxyhydroxide deposits at a slow-spreading centre with thickened oceanic crust: the Lilliput hydrothermal field (9°33′S, Mid-Atlantic Ridge). Chem. Geol. 278, 186–200.

Dill, H.G., Siegfanz, G., Marchig, V., 1994. Mineralogy and chemistry of metalliferous muds forming the topstratum of a massive sulfide- metalliferous sediment sequence from East Pacific Rise 18°S: its origin and implications concerning the formation of ochrous sediments in Cyprus-type deposits. Mar. Georesour. Geotechnol. 12 (2), 159–180.

Douville, E., Bienvenu, P., Charlou, J.L., Donval, J.P., Fouquet, Y., Appriou, P., Gamo, T., 1999. Yttrium and rare earth elements in fluids from various deep-sea hydrothermal systems. Geochim. Cosmochim. Acta 63 (5), 627–643.

Dymond, J., Eklund, W., 1978. A microprobe study of metalliferous sediment components. Earth Planet. Sci. Lett. 40 (2), 243–251.

Emerson, D., Moyer, C.L., 2002. Neutrophilic Fe-oxidizing bacteria are abundant at the loihi seamount hydrothermal vents and play a major role in Fe oxide deposition. Appl. Environ. Microbiol. 68 (6), 3085–3093.

Emerson, D., Fleming, E.J., Mcbeth, J.M., 2010. Iron-oxidizing bacteria: an environmental and genomic perspective. Annu. Rev. Microbiol. 561–579.

Ferris, F.G., 2005. Biogeochemical properties of bacteriogenic iron oxides. Geomicrobiol. J. 22, 79–85.

Fortin, D., Ferris, F.G., Scott, S.D., 1998. Formation of Fe-silicates and Fe-oxides on bacterial surfaces in samples collected near hydrothermal vents on the Southern Explorer Ridge in the northeast Pacific Ocean. Am. Mineral. 83 (11), 1399–1408.

Geist, D., Diefenbach, B.A., Fornari, D.J., Kurz, M.D., 2006. Construction of the Galápagos platform by large submarine volcanic terraces. Geochem. Geophys. Geosyst. 9 (3). http://dx.doi.org/10.1029/2007GC001795.

Grill, E.V., Chase, R.L., MacDonald, R.D., Murray, J.W., 1981. A hydrothermal deposit from Explorer Ridge in the northeast Pacific Ocean. Earth Planet. Sci. Lett. 52 (1), 142–150.

Harder, Hermann, 1978. Synthesis of iron layer silicate minerals under natural conditions. Clays Clay Miner. 26 (1), 65–72.

Hekinian, R., Rosendahl, B.R., Cronan, D.S., Dmitriev, Y., Fodor, R.V., Goll, R.M., Hoffert,

M., Humphris, S.E., Mattey, D.P., Natland, J., Peterson, N., Roggenthen, W., Schrader, E.L., Srivastava, R.K., Warren, N., 1978. Hydrothermal deposits and associated basement rocks from the Galapagos spreading center. Oceanol. Acta 1, 473–482.

Hoffert, M., Perseil, A., Hekinian, R., Choukroune, P., Needham, H.D., Francheteau, J., Le Pichon, X., 1978. Hydrothermal deposits sampled by diving saucer in transform fault A near 37°N on the Mid-Atlantic Ridge, famous area. Oceanol. Acta 1 (1), 73–86.

Jambor, J.L., Dutrizac, J.E., 1998. Occurrence and constitution of natural and synthetic ferrihydrite, a widespread iron oxyhydroxide. Chem. Rev. 98, 2549–2585.

Kelley, K.A., Plank, T., Ludden, J., Staudigel, H., 2003. Composition of altered oceanic crust at ODP Sites 801 and 1149. Geochem. Geophys. Geosyst. 4 (6), 8910.

Klein, E.M., Langmuir, C.H., Staudigel, H., 1991. Geochemistry of basalts from the southeast Indian Ridge, 115°E – 138°E. J. Geophys. Res. 96, 2089–2107.

Köhler, B., Singer, A., Stoffers, P., 1994. Biogenic nontronite from marine white smoker chimneys. Clay Clay Miner. 42 (6), 689 (70).

Li, J., Zhou, H., Peng, X., Wu, Z., Chen, S., Fang, J., 2012. Microbial diversity and biomineralization in low-temperature hydrothermal iron-silica-rich precipitates of the Lau Basin hydrothermal field. FEMS Microb. Ecol. 81, 205–216.

McMurtry, G.M., Sedwick, P.N., Fryer, P., Vonderhaar, D.L., Yeh, H.W., 1993. Unusual geochemistry of hydrothermal vents on submarine arc volcanoes: Kasuga Seamounts, Northern Mariana Arc. Earth Planet. Sci. Lett. 114 (4), 517–528.

Monecke, T., Petersen, S., Lackschewitz, M., Hugler, M., Hannington, M., Gemmel, J., 2009. Shallow submarine hydrothermal systems in the Aeolian volcanic arc, Italy. EOS 90 (13), 110–111.

Murnane, R., Clague, D.A., 1983. Nontronite from a low-temperature hydrothermal system on the Juan de Fuca Ridge. Earth Planet. Sci. Lett. 65, 343–352.

O'Connor, J.M., Stoffers, P., Wijbrans, J.R., Worthington, T.J., 2007. Migration of widespread long-lived volcanism across the Galapagos Volcanic Province: evidence for a broad hotspot melting anomaly? Earth Planet. Sci. Lett. 263, 339–354.

Petersen, S., et al., 2008. Drilling submarine hydrothermal systems in the Tyrrhenian Sea, Italy. InterRidge News 17, 21–23.

Pichler, T., Veizer, J., 1999. Precipitation of Fe(III) oxyhydroxide deposits from shallow-water hydrothermal fluids in Tutum Bay, Ambitle Island, Papua New Guinea. Chem. Geol. 162, 15–31.

Severmann, S., Mills, R.A., Palmer, M.R., Fallick, A.E., 2004. The origin of clay minerals in active and relict hydrothermal deposits. Geochim. Cosmochim. Acta 68 (1), 73–88.

Sinton, C.W., Christie, D.M., Duncan, R.A., 1996. Geochronology of Galapagos seamounts. J. Geophys. Res.: Solid Earth 101 (B6), 13689–13700.

Stoffers, P., Singer, A., McMurtry, G., Arquit, A., Yeh, H.W., 1990. Geochemistry of a hydrothermal nontronite deposit from the Lau Basin, Southwest Pacific. Geol. Jahrb. D 92, 615–628.

Sun, S.S., McDonough, W.F., 1989. Chemical and Isotopic Systematics of Oceanic Basalts: Implications for Mantle Composition and Processes 42. Geological Society, London, pp. 313–345.

Tivey, M.K., 2007. Generation of seafloor hydrothermal vent fluids and associated mineral deposits. Oceanography 20 (1), 50–65. http://dx.doi.org/10.5670/oceanog.2007.80.

Ueshima, M., Tazaki, K., 2001. Possible role of microbial polysaccharides in nontronite formation. Clays Clay Miner. 49 (4), 292–299.